Supplementary Materials for

Observation of a Chiral Wave Function in Twofold degenerate Quadruple Weyl System BaPtGe

S.1 Methods

Sample preparation and characterizations: To grow BaPtGe single crystals, all the elements were stored and manipulated in an argon-filled glovebox with moisture and oxygen levels less than 0.1 ppm. Samples were prepared by the In-flux method. The high-purity Ba (lumps), Pt (powder), Ge (lumps), and In (grains) were put into a corundum crucible. The charged crucible and another catching crucible were sealed into a Ta tube with partially filled Ar gas. The Ta tube was sealed into quartz tube in order to avoid oxidation at high temperature. The tube was heated to 1180 °C in 12 h and held there for another 12 h. Then the ampoule was cooled down to 900 °C at a rate of ~ 2.5 °C/h. At this temperature, the flux was removed by centrifugation to obtain the shiny cubic-like crystals. The X-ray diffraction pattern of a BaPtGe single crystal was measured using a Bruker D8 X-ray diffractometer with Cu Kα radiation (λ = 0.15418 nm) at room temperature. The elemental analysis was performed using energy-dispersive X-ray spectroscopy analysis in a FEI Nano 450 scanning electron microscope. No significant deviations from the expected structure and stoichiometry were observed in either measurement. The sample size is ~0.5×0.5×0.04 mm^3. The sample was thinned down to 40 μm using a polishing machine.

Inelastic x-ray scattering: The experiments were conducted at beam line 30-ID-C (HERIX) at the Advanced Photon Source (APS) [54]. The highly monochromatic x-ray beam of incident energy E_i = 23.7 keV (λ = 0.5226 Å) was focused on the sample with a beam cross section of ~35 × 15 μm^2 (horizontal × vertical). The overall energy resolution of the HERIX spectrometer was

ΔE ~ 1.4 meV (full width at half maximum). The measurements were performed in transmission geometry with temperature maintained at 300K. Typical counting times were in the range of 120 to 240 seconds per point in the energy scans at constant momentum transfer **Q**. H, K, L are defined in the cubic structure (space group #198 $P2_13$) with a=b=c=6.747 Å at room temperature. In our experimental condition, the self-absorption effect is small (Fig. S1), and hence neglected.

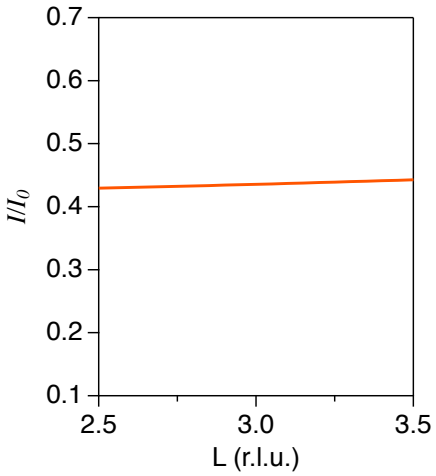

Fig. S1. Calculated self-absorption effect from Q=(0,3,2.5) to (0,3,3.5) (r.l.u). The self-absorption effect is described by: $\frac{I}{I_0} = \frac{sin\theta_o}{sin\theta_i + sin\theta_o}\left(1 - exp\left[-t\mu\left(\frac{1}{sin\theta_i} + \frac{1}{sin\theta_o}\right)\right]\right)$, where I and I_0 are scattering intensities with and without self-absorption, θ_i and θ_o are the angle of incidence and exit with respect to the sample surface, μ=1/40 μm^{-1} is the absorption coefficient and t=40 μm is the thickness of the sample. The intensity variation from the absorption effect across the Brillouin zone is less than 3% and smaller than the statistical errors (>5%). The excellent consistency between the IXS and DFT result (see main text) also confirms the negligible intensity variation due to experimental geometry change.

Density functional theory calculation of phonon spectrum: The phonon dispersions of BaPtGe were calculated using the density functional perturbation theory (DFPT) method and the Vienna Ab initio Simulation Package (VASP). The exchange-correlation potential was treated within the generalized gradient approximation (GGA) of the Perdew-Burke-Ernzerhof variety, where the

kinetic energy cutoff was set to 400 eV. Integration for the Brillouin zone were done by using Monkhorst-Pack *k*-point grids which is equivalent to 8×8×9.

Definition of pseudospin: The Hamiltonian of the TQW (Eq. 1 in main text) can be written as $H_{2\times2}(\mathbf{q}) = f_{i=x,y,z}(\mathbf{q}) \cdot \sigma_{i=x,y,z}$, where $\sigma_{x,y,z}$ are the Pauli matrices. This means that the wavefunctions can be characterized by their pseudospin, which is defined as $\hat{S}_i \equiv \frac{f_i(\mathbf{q})}{|f_i(\mathbf{q})|}$, where i is a Cartesian index. This gives:

$$\hat{S}_x = \frac{f_x}{|f_x^2+f_y^2+f_z^2|} = \frac{q_z^2-\frac{1}{2}(q_x^2+q_y^2)}{|f_x^2+f_y^2+f_z^2|} \qquad (1)$$

$$\hat{S}_y = \frac{f_y}{|f_x^2+f_y^2+f_z^2|} = \frac{\frac{\sqrt{3}}{2}(q_x^2-q_y^2)}{|f_x^2+f_y^2+f_z^2|} \qquad (2)$$

$$\hat{S}_z = \frac{f_z}{|f_x^2+f_y^2+f_z^2|} = \frac{q_x q_y q_z}{|f_x^2+f_y^2+f_z^2|} \quad . \qquad (3)$$

Along each diagonal direction, such as the eight R-points, $\hat{S}_x = \hat{S}_y \equiv 0$, leaving only a single component of $\hat{S}_z = \pm 1$. Thus, pseudospins will point to $\pm q_z$ at eight R points, and the sign of $\hat{S}_z$ is only determined by the coordinate of the R point, i.e., the sign of $q_x q_y q_z$.

Chern number calculation: The flux of Berry curvature, i.e., Chern number, is defined on a sphere that closed the Weyl node, and is calculated by discretizing the sphere into several horizontal circles with parameters, θ and Ψ, as shown in Fig. S2 (a). The one-dimension loop θ_i accumulates a Berry phase when Ψ is integrated from 0 to 2π and corresponds to an average position charge, ⟨Ψ⟩. ⟨Ψ⟩ can only shift by $2N\pi$ when θ varies from 0 to π, where N is the Chern number of the Weyl node enclosed. The sign of N gives the chirality information of the Weyl node. Fig. S2 (b) is the Berry curvature calculation for the 4th band around Γ. The charge center ⟨Ψ⟩ have a 8π shift from θ=0 to π, which gives the Chern number of C = +4. Similarly, we calculated the charge center ⟨Ψ⟩ of the 5th band and obtained C = -4.

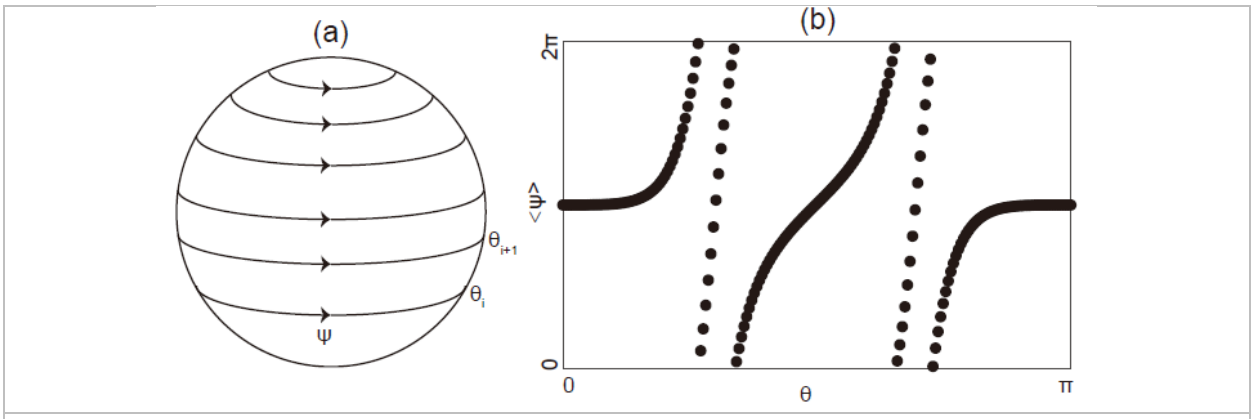

Fig. S2. (a) Sample selection of *k* points to calculate the Chern number. (b) Chern number calculation for the twofold quadruple Weyl node by Wilson loop method, with the k-points in (a).

Phase choice of the wave functions: In quantum mechanics, the wave function allows an arbitrary global phase $\varphi = e^{i\theta}\varphi$ that keeps observables unchanged. In our manuscript, all calculations and model analysis have used a convention that the $e^{j}_{dx}(q = 0)$ component has a phase of zero.

S.2 Sample characterization

Fig. S3a shows an x-ray diffraction (XRD) pattern from the [110] face of our BaPtGe single crystal. All peaks can be indexed as the (*hh*0) reflections of BaPtGe. The chemical composition of BaPtGe is confirmed by the EDX spectrum (Fig. S3b). The EDX results indicate that the distributions of elements Ba, Pt and Ge are homogenous from point to point. The average atomic ratio of Ba: Pt: Ge is about 1.02: 0.98: 1 when setting the content of Ge as 1. No impurities were found except carbon and oxygen that were induced during the measurement process, suggesting that the sample is pure.

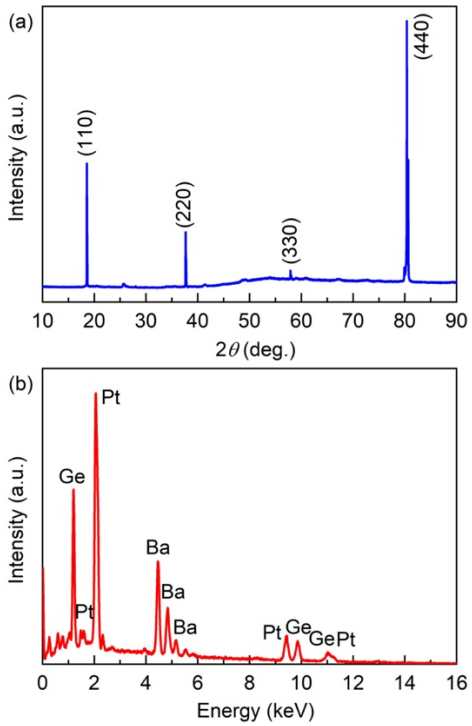

Fig. S3. (a) XRD pattern of a BaPtGe single crystal. (b) A representative EDX spectrum measured from a BaPtGe single crystal.

S.3 Inelastic x-ray scattering cross section

Here we briefly review the IXS cross-section. For solid angle $d\Omega$ and bandwidth $d\omega$ [55]

$$\frac{d^2\sigma}{d\Omega \mathrm{d}\omega} = \frac{k_f}{k_i} r_0^2 |\overrightarrow{\epsilon_i} \cdot \overrightarrow{\epsilon_f}|^2 S(\mathbf{Q}, \omega) \qquad (4)$$

where $\mathbf{k}$ and $\boldsymbol{\epsilon}$ represent the scattering vector and x-ray polarization and i and f denote initial and final states. r_0 is the classical radius of the electron. In a typical measurement, the energy transfer ω is much smaller than the incident photon energy (23.71 keV in our study) and the variation in $\overrightarrow{\epsilon_i} \cdot \overrightarrow{\epsilon_f}$ is relatively small. Therefore, the term $\frac{\boldsymbol{k_f}}{\boldsymbol{k_i}} \sim 1$, and $\frac{d^2\sigma}{d\Omega \mathrm{d}\omega} \propto S(\mathbf{Q}, \omega)$.

Under the linear response approximation, $S(\mathbf{Q},\omega)$ can be formulated as

$$S(\mathbf{Q}, \omega) = \frac{1}{2\pi\hbar} \int_{-\infty}^{\infty} dt\, e^{-i\omega t} \langle \rho(\boldsymbol{Q}, 0) \rho^{+}(\boldsymbol{Q}, t) \rangle \,. \quad (5)$$

This depends on the charge-density operator

$$\rho(\boldsymbol{Q},t)=\sum_{l}^{Primitive}\sum_{d}^{atoms}f_d(\boldsymbol{Q})e^{-i\boldsymbol{Q}\cdot\boldsymbol{r}_{ld}}e^{-i\boldsymbol{Q}\cdot\boldsymbol{u}_{ld}(t)} \quad (6)$$

where $\boldsymbol{r}_{ld}$ is the equilibrium atomic position and $\boldsymbol{u}_{ld}$ is the time-dependent displacement. $f_d(\boldsymbol{Q})$ is the atomic form factor of the d^{th} atom. Combining Eq. (5) and (6) gives

$$S(\mathbf{Q},\omega)=\frac{N_l}{2\pi\hbar}\sum_{l}^{Primitive}e^{-i\boldsymbol{Q}\cdot\boldsymbol{r}_l}\sum_{dd'}^{atoms}f_{d'}(\boldsymbol{Q})f_d(\boldsymbol{Q})e^{-i\boldsymbol{Q}\cdot(\boldsymbol{r}_{d'}-\boldsymbol{r}_d)}e^{-i\boldsymbol{Q}\cdot\boldsymbol{u}_{ld}(t)}\int_{-\infty}^{\infty}dt\,e^{-i\omega t}\langle e^{-i\boldsymbol{Q}\cdot\boldsymbol{u}_{0d'}(0)}e^{i\boldsymbol{Q}\cdot\boldsymbol{u}_{ld}(t)}\rangle. \quad (7)$$

By applying the Baker-Hausdorf theorem to expand $\langle e^{-i\boldsymbol{Q}\cdot\boldsymbol{u}_{0d'}(0)}e^{i\boldsymbol{Q}\cdot\boldsymbol{u}_{ld}(t)}\rangle$, we obtain

$$S(\mathbf{Q},\omega)=S_{0p}(\mathbf{Q},\omega)+S_{1p}(\mathbf{Q},\omega)+S_{2p}(\mathbf{Q},\omega)+\cdots \quad (8)$$

Where $S_{0p}(\mathbf{Q},\omega)$ corresponds to elastic Bragg scattering. For the inelastic part, higher order process, such as the two-phonon $S_{2p}(\mathbf{Q},\omega)$ term, are usually much weaker than the one phonon process. Therefore, in our calculations, we only consider the one-phonon term that can be expressed as

$$S_{1p}(\boldsymbol{Q},\omega)=N_l\sum_{q}^{BZ}\sum_{j}\frac{1}{\omega_{qj}}\left|\sum_{d}\frac{f_d(\boldsymbol{Q})}{\sqrt{2M_d}}e^{-W_d}\boldsymbol{Q}\cdot\boldsymbol{e}_d^{j}(\boldsymbol{q})\,e^{i\boldsymbol{Q}\cdot\boldsymbol{r}_d}\right|^2\delta_{\boldsymbol{Q}-\boldsymbol{q},G}\begin{Bmatrix}\langle n_{\omega_{qj}}+1\rangle\,\delta(\omega-\omega_{qj})\\ \langle n_{\omega_{qj}}\rangle\,\delta(\omega+\omega_{qj})\end{Bmatrix} \quad (9)$$

Here the Debye-Waller factor W_d is a smooth and flat function within one BZ and hence also neglected in our first-principle calculations.

To make a direction comparison between theoretical calculations and experiment, we convolute $S_{1p}(\boldsymbol{Q},\omega)$ with the experimental resolution which has a pseudo-voigt shape

$$R(\omega)=(1-\alpha)\frac{I}{\sqrt{2\pi}\sigma}e^{-\frac{\omega}{2\sigma^2}}+\alpha\frac{I}{\pi}\frac{\Gamma}{\omega^2+\Gamma^2} \quad (10)$$

where the energy resolution is characterized by the full-width-at-half-maximum (FWHM) of this function. The $S_r^{DFT}(\mathbf{Q},\omega)$ shown in the main text is calculated from

$$S^{DFT}(\mathbf{Q}=\mathbf{q}+\mathbf{G},\omega)=\sum_{j}\frac{1}{\omega_{qj}}\left|\sum_{d}\frac{f_d(\boldsymbol{Q})}{\sqrt{2M_d}}\boldsymbol{Q}\cdot\boldsymbol{e}_d^{j}(\boldsymbol{q})\,e^{i\boldsymbol{Q}\cdot\boldsymbol{r}_d}\right|^2\begin{Bmatrix}\langle n_{\omega_{qj}}+1\rangle\,\delta(\omega-\omega_{qj})\\ \langle n_{\omega_{qj}}\rangle\,\delta(\omega+\omega_{qj})\end{Bmatrix}\otimes R(\omega) \quad (11)$$

S.4 Directional wave function

Figure 2 of the main text shows DFT calculated $S^{DFT}(\boldsymbol{Q},\omega), R(\boldsymbol{Q},\omega)$ and $I(\boldsymbol{Q},\omega)$ along the high-symmetry R_1(-0.5, 2.5, 2.5)-Γ(0, 3, 3)-R_2(0.5, 3.5, 3.5) direction. Here we show the same plots but along the X_1(0, 3, 2.5)-Γ-X_2(0, 3, 3.5), M_1(0, 2.5, 2.5)-Γ-M_2(0, 3.5, 3.5) directions in Fig. S4. Unlike the [111] direction, where $S^{DFT}(\boldsymbol{Q},\omega)$ near the TQW is dominated by the imaginary component of the wave functions, along [001] and [011] directions, the wave functions near the TQW are purely real, in agreement with our model calculations.

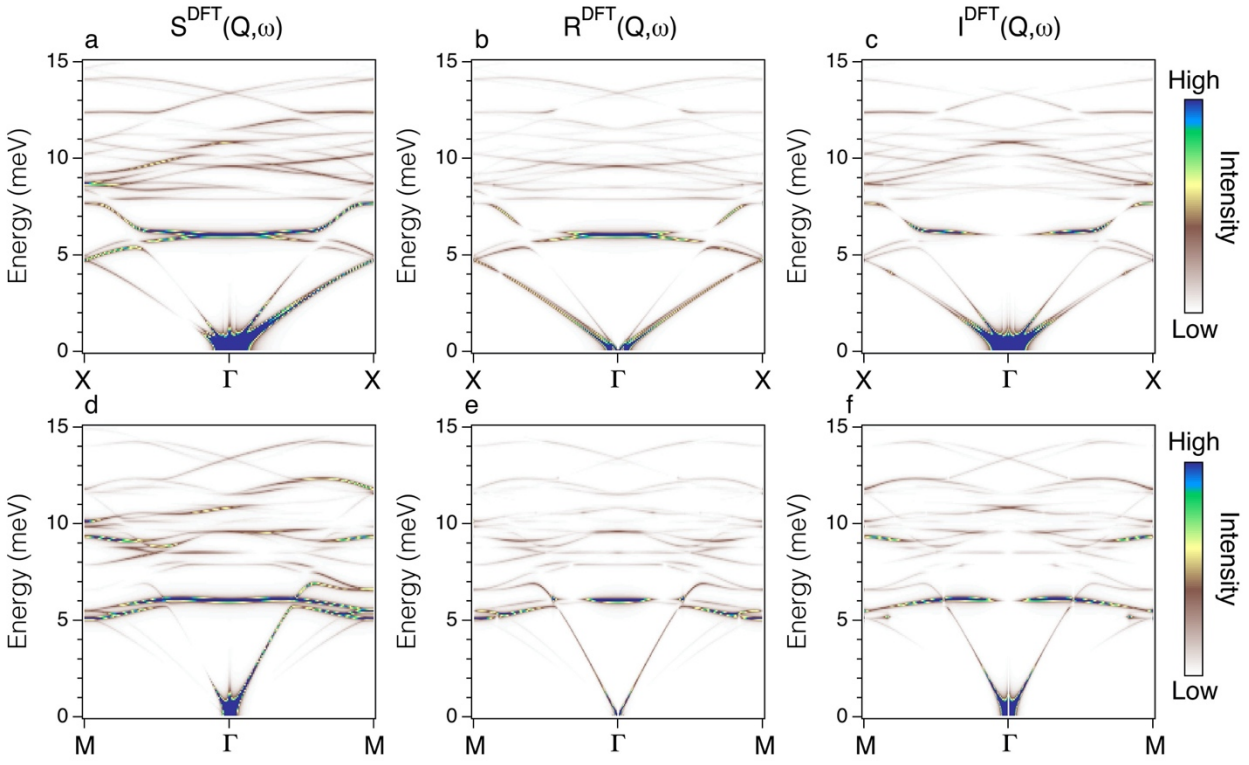

Fig. S4. DFT calculated $S^{DFT}(\boldsymbol{Q},\omega), R(\boldsymbol{Q},\omega)$ and $I(\boldsymbol{Q},\omega)$ along the [001] (panel a-c) and [011] (panel d-f) directions. Since the effective TQW Hamiltonian is derived based on symmetries at the Γ point, I(Q,ω) along [001] and [011] directions are zero only near the Γ point.

S.5 Peak position and intensity extractions

The peak positions shown in Fig. 4a-c in the main text are extracted by analyzing the derivatives of smoothed data at each constant-momentum-transfer cut of $S^{exp}(\mathbf{Q}, \omega)$ presented in Fig. 3. The peak center is found where the derivative of the smoothed spectrum crosses zero. This method provides a direct and model-independent way to trace the peak dispersions in $S^{exp}(\mathbf{Q}, \omega)$. Fig. S5 shows the extracted peak positions overlaid on the measured $S^{exp}(\mathbf{Q}, \omega)$, offering a direct comparison between the peak tracing result to the raw data. The extracted peak centers display an excellent overall quality of tracing the major dispersive features in the spectra, especially the TQW bands at ~6 meV, which yield the dominant spectral intensity. The spectral intensity of the TQW bands shown in Fig. 4d-f is the corresponding peak intensity value at each peak center.

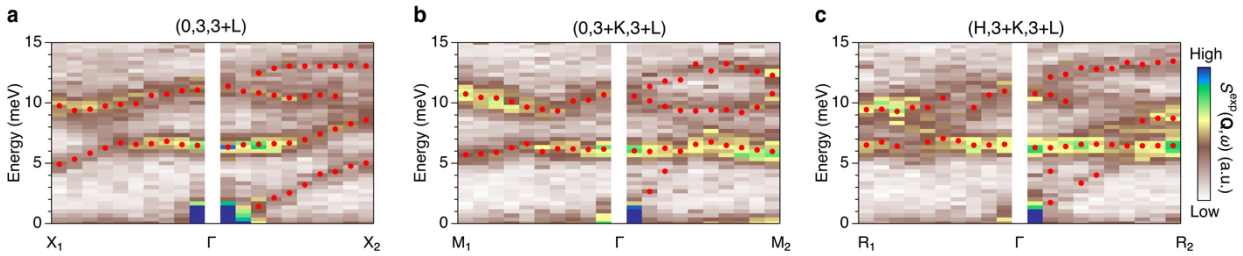

Fig. S5. The extracted peak positions overlaid on the measured $S^{exp}(Q, \omega)$.

S.6 TQW band crossing

Figure S6a-b show the two dispersive arms of the TQW bands along Γ-X (raw IXS data shown in Fig. 3a). The black squares trace the peak position of the Weyl bands downward (towards lower energy, panel a) and upward (towards higher energy, panel b). Although the spectral feature of the Weyl node is asymmetric around Γ (Fig. 3a), due to the chiral wave function, the complete shape

of the Weyl node can be shown by the symmetrized peak loci (Fig. S6c) and the symmetrized spectrum (Fig. S6d).

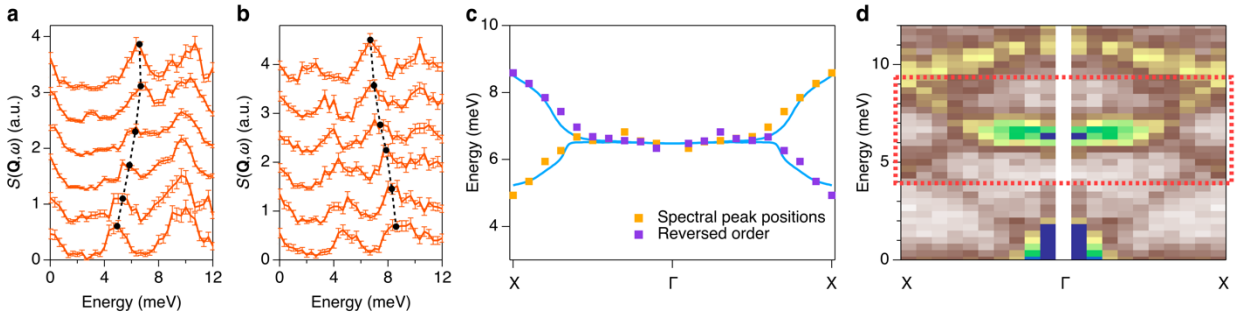

Fig. S6. Quadruple Weyl node. (**a-b**) Constant momentum cut $S(\mathbf{Q},\omega)$ of the dispersive part of the quadruple Weyl nodes as shown in Fig. 3a in the main text. Panel **a** from top to bottom: (0,3,2.75) to (0,3,2.5); Panel **b** from top to bottom: (0,3,3.25) to (0,3,3.5). (**c-d**) The extracted peak dispersion (yellow squres) of the quadruple Weyl node along Γ-X. The purple squares present the symmetrized dispersion. (**d**) The symmetrized spectrum of $S(\mathbf{Q},\omega)$ shown in Fig. 3(a).

S.7 TQW in FeSi

Since TQW is protected by chiral cubic and time-reversal symmetry, it can also be realized in other materials [32]. An interesting case is FeSi, which has the same space group of BaPtGe [12]. The calculated $S^{DFT}(q,\omega)$ of FeSi and BaPtGe along [0,0,1]-[0,0,3] direction are shown in Fig. S7 (a) and (b), respectively. Similar to BaPtGe, the TQW node is also formed by the 4th band and 5th band, as marked by the red and blue circles. However, the Chern numbers of the two phonon bands are reversed comparing with the case in BaPtGe, *i.e.*, the 4th band has C=-4 in FeSi but C=+4 in BaPtGe. Consequently, the relative intensity between the 4th and 5th band is reversed. This observation, once again, proves that IXS intensity is sensitive to the chirality.

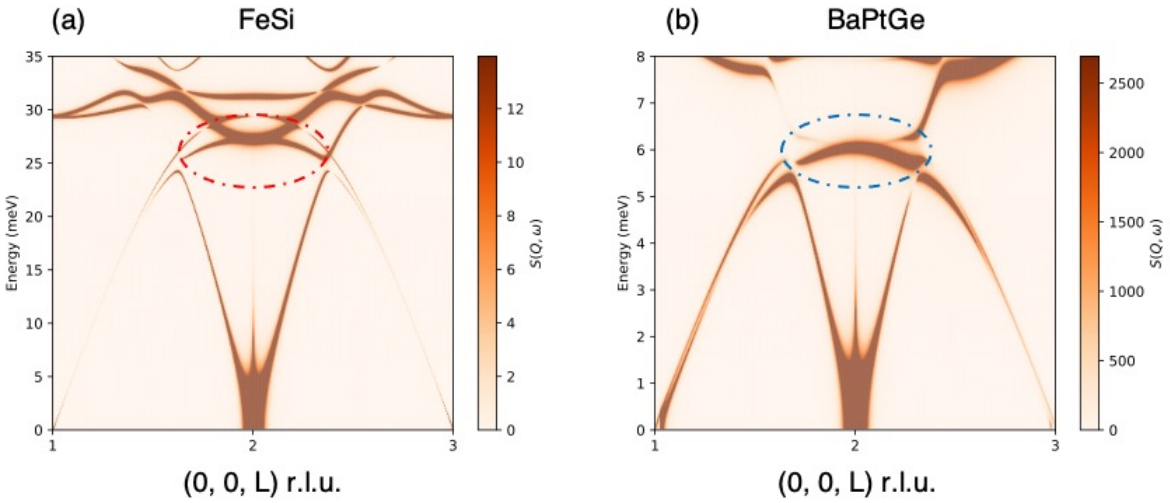

Fig. S7. Calculated S^{DFT}(q,w) of (a) FeSi and (b) BaPtGe along [0,0,1]-[0,0,3] direction. The TQW nodes are marked by red and blue circles in (a) and (b), respectively.

S.8 Double Weyl nodes in BaPtGe

Phonon spectra and density of states of BaPtGe are shown in Fig. S8, where the purple solid dots mark the twofold quadruple Weyl nodes. Due to the protection arising from chiral cubic symmetry, threefold nodes in the optical branches at Γ points are all threefold double Weyl nodes, which are also known as spin-1 Weyl nodes, having Chern numbers of C = +1, 0, -1 for each band. We note that the threefold degenerate nodes at the Γ points that are formed by the acoustic bands are also spin-1 Weyl nodes. The low-energy effective model for the threefold Weyl node is:

$$H_{3\times3} = A\begin{pmatrix} 0 & ik_z & -ik_y \\ -ik_z & 0 & ik_x \\ ik_y & -ik_x & 0 \end{pmatrix} \qquad (12)$$

where A is a real constant. Due to the existence of C_2' screw rotation symmetry, all bands are fourfold Weyl nodes at R point, also known as charge-2 Dirac point. The low-energy effective model for the fourfold Weyl node is:

$$H_{4\times4} = B\begin{pmatrix} -k_x & k_z + ik_y & 0 & 0 \\ k_z - ik_y & k_x & 0 & 0 \\ 0 & 0 & k_x & -k_z + ik_y \\ 0 & 0 & -k_z - ik_y & -k_x \end{pmatrix} \quad (13)$$

where B is also a real constant. We marked all threefold and fourfold double Weyl nodes detected by IXS with dashed rectangular boxes in Fig. S8.

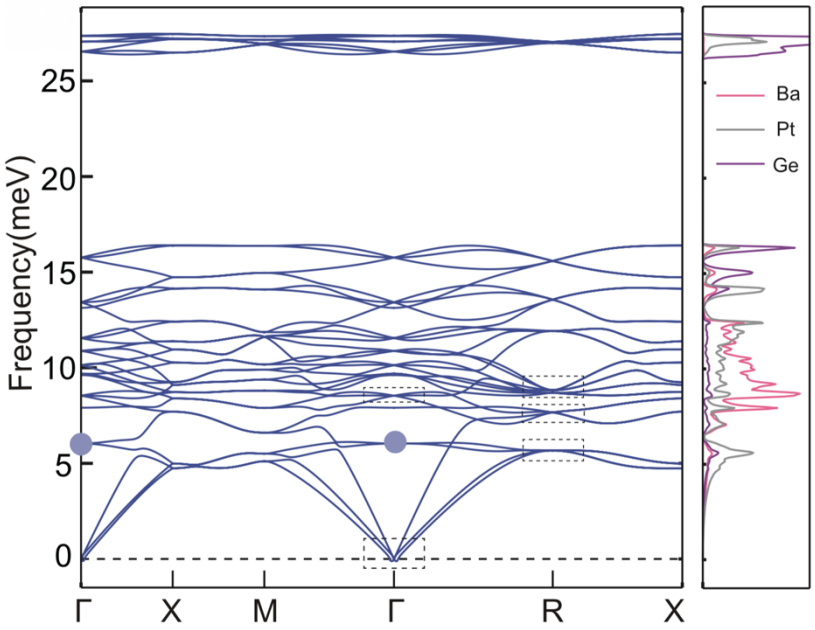

Fig. S8. Phonon spectra pf BaPtGe. Threefold nodes at Γ point marked by dashed rectangles are threefold double Weyl nodes detected by IXS, known as spin-1 Weyl nodes. Fourfold nodes at R points marked by dashed rectangles are fourfold double Weyl nodes detected by IXS, known as charge-2 Dirac nodes.

S.9 Consequences of the TQW and Symmetry breaking effect

The experimentally determined chiral phononic wave function of TQW has important consequences. Due to the high *C*, four chiral surface modes will emanate from the TQW (Fig. S9a) and may give rise to larger measurable physical quantities such as thermal Hall effect [40,41]. Another interesting property is that a topological phase transitions can be induced by applying

tensile strain along the [001] direction. In such case, the cubic lattice with space group #198 will transition to an orthorhombic lattice with space group #19, and hence break TQW into four conventional Weyl nodes with $|C|=1$ (Fig. S9b and S9d). Along with the topological transition, the bulk wave function will change and yield different pseudospin structure, as shown in Fig. S9. Further increasing the strain will push the four conventional Weyl nodes moving closer to their negative chirality pairs and annihilate eventually. This procedure demonstrates an external field control of the surface arcs.

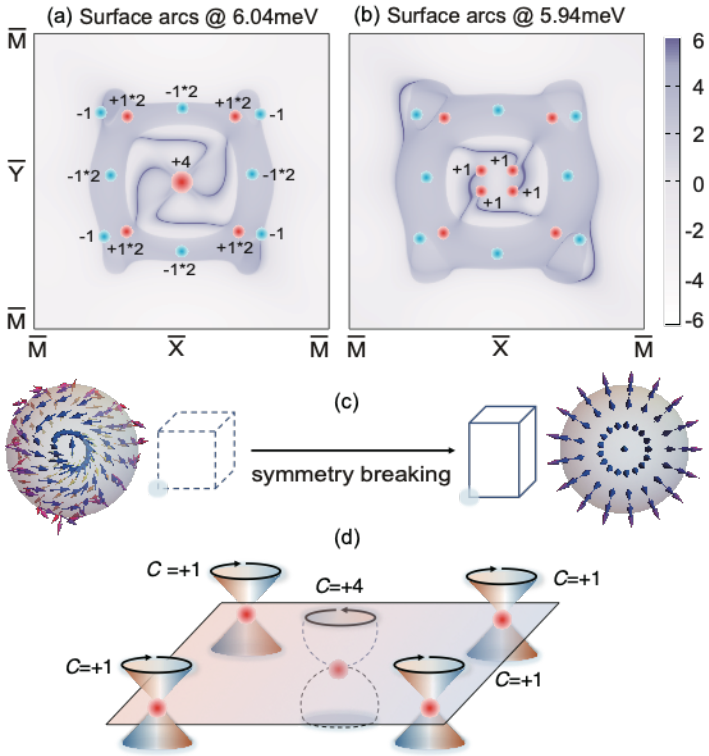

Fig. S9. Pressure induced topological phase transition. (a) Four topological phonon arcs are emitting from TQW. (b) Break the cubic symmetry will split TQW into four conventional Weyl nodes with $C=1$ and reduce the length of the phonon arcs. (c) Pseudo-spin texture at the R point before and after symmetry breaking. (d) Schematically depicts how TQW splits to four conventional Weyl nodes.

S.10 Atomic vibration animation for TQW

In this section we display the chirality of Weyl phonons directly by plotting their wave functions. In the attachment, we provide animations of the 4^{th} and 5^{th} index modes, which correspond to the TQW at $\mathbf{q}$ = (0.05, 0.05, 0.05) in reciprocal lattice unit. Since all atoms move, the full displacement patterns are somewhat complicated. The chiral properties of the modes are most apparent by focusing on the Pt atoms, which rotate around the [111] direction with right/left-handed chirality.

References:

[54] A. H. Said, H. Sinn, T. S. Toellner, E. E. Alp, T. Gog, B. M. Leu, S. Bean and A. Alatas, High-energy-resolution inelastic X-ray scattering spectrometer at beamline 30-ID of the Advanced Photon Source, J. Synchrotron Rad. **27**, 827-835 (2020).

[55] A. Q. R. Baron, High-Resolution Inelastic X-Ray Scattering II: Scattering Theory, Harmonic Phonons, and Calculations. *Synchrotron Light Sources and Free-Electron Lasers* 1721–1757 (2016). doi:10.1007/978-3-319-14394-1_52.